On-orbit alignment and imaging performance of the HST Advanced Camera for Surveys

G.F. Hartig[a], J.E. Krist[a], A.R. Martel[b], H.C. Ford[b], G.D. Illingworth[c]

[a] Space Telescope Science Institute, 3700 San Martin Drive, Baltimore, MD 21218
[b] Department of Physics and Astronomy, Johns Hopkins University
[c] Lick Observatory, UCSC

ABSTRACT

The Advanced Camera for Surveys (ACS), installed in the Hubble Space Telescope in March 2002, has significantly extended HST's imaging capabilities. We describe the on-orbit optical alignment procedures and results, detailing the excellent image quality performance achieved. Comparison is made with the instrument specifications, ground test results and published performance expectations. The residual aberration content over the field of each channel is described and compared with the optical model, and various other performance measures, including sharpness and encircled energy are treated. The effects of the telescope focus oscillations due to thermal variations ("breathing") and image positional stability are also discussed.

Keywords: HST, ACS, optical alignment, image quality, image stability

1. INTRODUCTION

The Advanced Camera for Surveys, recently installed in the HST observatory, is a multi-purpose imager designed expressly to enhance the survey mode discovery efficiency of the HST by more than a magnitude, while providing a variety of additional capabilities for more targeted science programs. The ACS design and science objectives are detailed by Ford, et al..[1-3] Briefly, the camera consists of three optical channels, each optimized for specific wavelength coverage, field size and spatial resolution requirements of the ACS science programs. The wide field channel (WFC), intended for survey work in the visible and near IR, covers an area of the sky over 200 arcsec square with 50 milli-arcsec pixels on a pair of butted 4Kx2K CCDs.[4] This high efficiency detector, together with the excellent optical throughput provided by the 3 mirror optical design and enhanced silver coatings, and the wide sky coverage, yield an order of magnitude improvement in discovery efficiency over the current HST wide field camera (WFPC2).[3,5,6] The high resolution channel (HRC) employs a 1K square CCD to cover a 26 arcsec square field, from the near UV through near IR, and includes an aberrated beam coronagraphic capability, which permits high contrast studies within about 1 arcsec of bright point sources.[7] Finally, the solar blind channel (SBC) uses a spare detector from the Space Telescope Imaging Spectrograph (STIS) program to provide far UV imaging capability over a field of about 31 arcsec square.[8]

After a 7 year design, development and integration program followed by an extensive ground verification and calibration test phase, the ACS was launched aboard shuttle Columbia on STS-109, the fourth servicing mission to the HST, on 1 March, 2002, and was installed in the observatory 6 days later. After the HST was released by the shuttle on 10 March, the servicing mission observatory verification (SMOV) program commenced and ACS successfully underwent an exhaustive series of tests and calibrations which have demonstrated nominal performance in nearly all aspects. ACS has now been fully commissioned for general observer utilization and is operating as expected.[5,6]

This paper describes the optical alignment procedures used to optimize the image quality on orbit and the resulting optical performance, as assessed by a series of SMOV observations. We begin with a brief description of the optical-mechanical design and its features which permit the alignment of the camera with respect to the HST optical telescope assembly (OTA). Results of the subsequent SMOV tests of image quality over the fields of each of the three ACS channels are presented, with comparison to the ground test analyses and performance specifications. We then treat the stray light performance, describing several ghost image and scattered light features, their origins and intensities. We conclude with a discussion of the stability of the images produced by OTA-ACS system. Excluded from this discussion

is the performance of the ACS aberrated beam coronagraph mode, which is described by Krist, et al.[7]. Verification of the grism low-resolution disperser mode is described separately by Walsh, et al.[9]

2. ACS OPTICAL DESIGN

The ACS WFC achieves its goal of improving the HST discovery efficiency, defined as the product of field area and throughput, by a factor of > 10, by utilizing a novel optical design which makes full use of the field available to an axial HST science instrument and maximizes efficiency. The design has been described in detail by its chief architect, R. Woodruff.[10] Just three mirrors, each with an enhanced silver coating for optimal reflectance in the 400-1100 nm passband of the WFC, are used to correct the OTA aberrations and produce diffraction-limited performance over the full 205 arcsec square field. The first mirror, a concave sphere, is mounted on an alignment corrector mechanism, which permits angular adjustment of the mirror in 2 axes, such that the OTA pupil may be accurately registered on the second mirror, an anamorphic asphere, which corrects the OTA spherical aberration and astigmatism at field center. The third mirror, used at nearly 45 degrees, is a 3rd order Schmidt plate, which corrects the field dependent astigmatism. The corrector mechanism also permits focus adjustment. The evacuated detector housing incorporates two fused silica windows, each with broadband anti-reflection coatings, and nearly normal to the chief ray. The outer window serves as the vacuum interface, such that the focal plane assembly can be operated at its nominal thermo-electrically cooled (TEC) temperature in the lab environment. The thin inner window is mounted in a heat shield, which is cooled to about –50C by four 2-stage TECs; this design limits the radiative coupling to the warm detector environment and enables a single 4-stage TEC to maintain the CCD at –77C, at which its dark current is very low.

The HRC and SBC require only two mirrors to provide well-corrected images over their shared 26-31 arcsec fields, since the field-dependence of the OTA astigmatism is small enough that exact correction at the field center is sufficient. These mirrors employ Al-MgF_2 coatings, optimized for high reflectance at 122 nm. A third mirror, mounted on a simple rotating mechanism, is inserted to fold the beam to the HRC detector or removed from the path for illumination of the SBC detector. This fold mirror is also coated with Al-MgF_2 but optimized for reflectance at 200 nm. As in the WFC, the first mirror, a concave sphere, is mounted on a corrector mechanism which provides tip/tilt and focus adjustment. Both the HRC CCD and SBC MAMA detector assemblies are evacuated and sealed. The HRC window, nearly normal to the chief ray, is broadband anti-reflection coated with MgF_2; the MgF_2 SBC detector window is uncoated and lies at a 24 degree angle of incidence.

The ACS optical design results in significant geometrical distortion over each of its fields of view, due predominantly to focal plane tilts of 20 deg (WFC) and 31 deg (HRC/SBC). However, higher-order distortion is also present, and results in pixel area variations of up to 19% (WFC) and ~3.5% (HRC/SBC). These have been calibrated and fitted with 4th order two-dimensional polynomials to provide corrections accurate to a small fraction of a pixel over the field.[11]

Although the ACS was carefully tested on the ground with well-verified opto-mechanical simulators of the HST OTA,[12,13] there remained significant uncertainties regarding its alignment on-orbit in the HST, necessitating the corrector mechanisms described above. Latch location and actuation uncertainties, launch vibration, and gravity release may all affect the optical alignment and produce unacceptable image quality degradation if not corrected, so each of the HST replacement science instruments has employed mechanisms to permit pupil alignment and focus adjustment. Because of the larger mass of the ACS WFC pupil-imaging mirror (due to the large field), the mechanism designs used for the earlier instruments were not suitable and a stiffer mechanism was developed. This employed a pair of nested, eccentric cylinders rotating on precision bearings and driven with geared stepper motors to achieve the angular positioning with ~2 arcsec steps in tip or tilt over a range of +/-5 arcmin. This “wobbler” mechanism rides on a set of rails with linear ball bearings and is driven by a stepper motor and lead screw/nut arrangement to effect focus adjustment over a range of +/-5.5 mm.

3. ON-ORBIT ALIGNMENT

Astronomical "first light" was achieved for ACS on 22 March 2002, when it observed a field in the open cluster NGC 188 with both the WFC and HRC channels in the narrowband filter F660N. Stellar images exhibited significant coma and defocus, as shown in Fig 1. Phase retrieval analysis[14] of several well-exposed stars in each field indicated .13 μm RMS of coma in both the WFC and HRC images, indicating pupil shear of about 600 μm or 2%. The defocus was estimated at ~ .9 mm at the OTA focal plane. The sense of the defocus was determined using exposures obtained at three settings of the ACS corrector focus, at +/- .5 mm from the nominal position. Both coma and defocus were readily correctable within <20% of the alignment mechanism range. Realtime commands were sent to the HST to effect the adjustments and the procedure was iterated twice to converge rapidly to the optimized images shown in Figure 2.

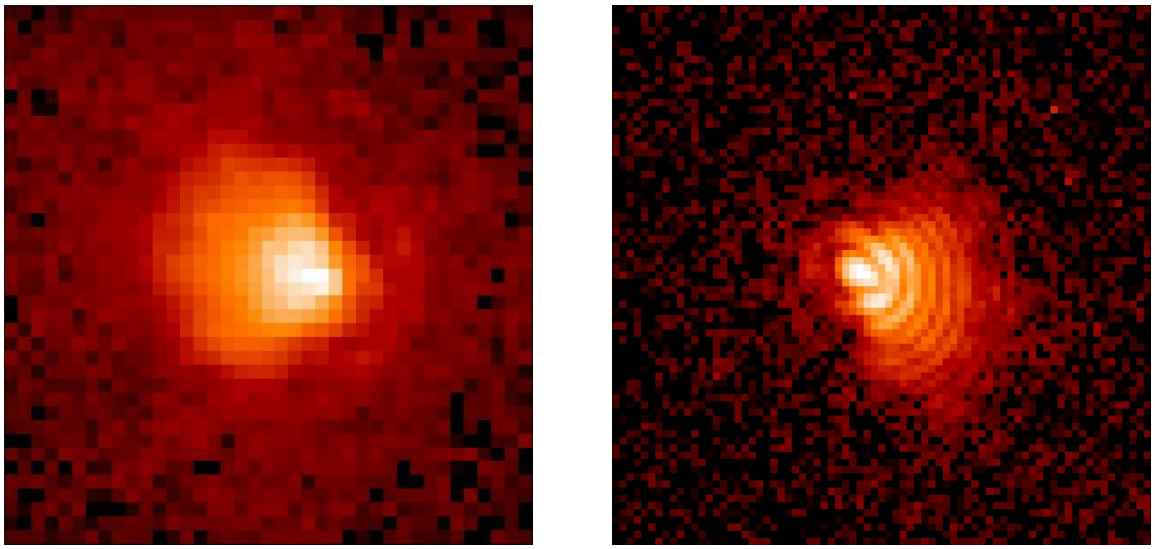

Figure 1. Star images from "first light" exposures through ACS. Both WFC (left) and HRC (right) exhibit similar coma (HRC format is inverted compared to WFC) and defocus. Frame width is 2.0 arcsec.

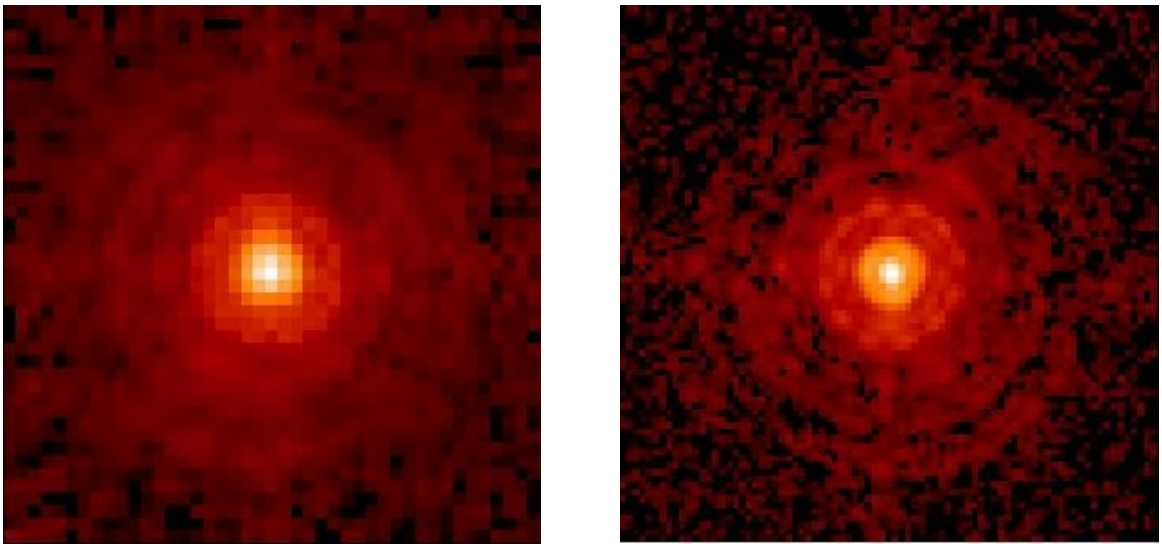

Figure 2. Images of same stars shown in figure 1, after alignment correction. Image quality specifications are readily met by both channels. Frame width is 2.0 arcsec .

To assure that the optimal pupil alignment and focus setting had been achieved, a second phase of the alignment procedure obtained images of the same field in NGC 188 at a series of closely spaced tip/tilt settings about the final adjustment from phase 1; an 8-position focus sweep was also performed. These resulted in only very small adjustments to achieve the final alignment state, in which the ACS has remained since 2 April 2002.

The OTA suffers from several defocus effects that complicate the setting of the ACS focus. The OTA metering structure, comprised of carbon fiber composite material, continues to shrink, presumably as a result of desorption, albeit at a rate that is much reduced from that seen in its first years on-orbit. Because the WFPC2 camera does not have an internal focus adjustment, the OTA secondary mirror despace is adjusted periodically to keep WFPC2 in focus. Thus, the ideal focus setting for the ACS makes it confocal with the WFPC2. A special set of concurrent observations was made with the ACS, STIS and WFPC2 to determine the optimal focus. These measurements, as are all HST observations, were subject to the OTA focus variation in response to thermal changes induced by the variation in solar illumination of the observatory as it moves into and out of the earth's shadow in its 96 minute orbit. Past correlation studies of various OTA temperatures with the defocus in WFPC2 images have provided a relative correction for this "breathing" effect over the course of an orbit, but have been unsuccessful in predicting the absolute defocus at any time. The final ACS focus adjustments placed both the WFC and HRC/SBC correctors 1.04 mm (-990 steps) aft of their ground-aligned positions.

The adjustments required to remove coma from both the WFC and HRC channels, the resultant image offsets from their nominal locations in the field and the focus offsets are all consistent with a simple rigid body displacement of the ACS with respect to its nominal location and orientation in the OTA and the uncertainties associated with the ground alignment. The similarities between the WFC and HRC channels preclude the loss of alignment of any single optic (due to launch vibration). One explanation for the initial on-orbit coma might be latch location uncertainty. The coma correction required tilts of each of the M1 mirrors by about 100 arcsec, indicating misalignment of about 200 arcsec from the expected orientation of ACS in the HST. If error in the position of the A latch, which most directly controls image location, is responsible for the image offset of about .7 mm (at the OTA focal plane) seen in both HRC and WFC, and the B latch is at its expected location, then the ACS axis will be tilted by about 150 arcsec from its pre-aligned orientation, which is similar in magnitude to the observed pupil shear. However, the actual required tilt correction was nearly perpendicular to the image offset direction, so B latch position error, compensating for the A latch error to remove the ACS tilt error in the image offset direction and producing the tilt error in the perpendicular direction, would be required.

An alternative explanation for the initial coma might be the effects of gravity release on the optical bench, particularly on the modified portion of the bench that supports the M2 mirrors (for both WFC and HRC/SBC channels), on which the OTA pupil is imaged. The similarity in coma seen in both channels lends credence to this explanation, although modeling indicated that gravity sag on the M2 mirrors should be much smaller than that required to produce the observed coma. The coronagraph performance also tends to refute this explanation, since the pupil mask appears to be very effective at suppressing the OTA spider diffraction, hence remains well centered on the pupil image. This mask is supported on the calibration door/coronagraph mechanism, which is attached to the optical bench in an entirely independent manner from the M2 mirror mounts.

It is most likely that a number of different effects contribute to the observed initial on-orbit misalignment, but they are small and well within the designed correction range.

4. IMAGE QUALITY OVER FIELD

After adjustment of the correctors, ACS image quality readily meets its image quality specifications in the WFC and HRC channels. The primary specification requires that greater than 75% of the energy from a point source be enclosed within a .25 arcsec diameter, EE(.25), at 633 nm, with a goal of 80%. Direct measurements of the encircled energy of star images through the F625W filter indicate that the goal has been readily achieved for the HRC, with EE(.25) = .82 (averaged over many images). The WFC easily meets the spec, and nears the goal, with an average EE(.25)=.79. These are similar to the EE values measured on the ground using the refractive aberrated simulator (RAS/HOMS) at Ball

Aerospace,[13] after final ACS integration in 2001. We attribute the difference in performance to the better sampling and superior MTF of the HRC detector.

In addition to the EE, we have investigated several other useful image quality metrics, and used them to evaluate the imaging performance of the ACS over each of its fields. Each metric has strengths and weaknesses as an indicator of the state of alignment or scientific performance:

Image width: The full width at half maximum (FWHM) of stellar images serves as a useful direct indicator of spatial resolution, and, if measured along orthogonal axes, the ratio can also indicate residual astigmatism or other asymmetrical aberrations. It is, however, subject to dependence on intra-pixel centration of the image and pixel-to-pixel sensitivity variations, when measured directly along slices through the image. This dependence may be mitigated for many purposes by fitting a sub-sampled 2-D gaussian to the image core, as we have done here.

Encircled energy: The fractional energy enclosed within a given area has been used for most of our ground and on-orbit alignment work. It is relatively insensitive to image centration, if fractional pixel contributions are approximated. The diameter over which the EE is computed must be selected carefully to maximize sensitivity to image quality while minimizing sensitivity to noise. We have typically used a diameter of .15 arcsec, which lies just outside the Airy disc for the ACS measurements at 633 nm. Absolute EE measurements must be careful to subtract the background properly, since small residuals integrate to significant fractions of the energy as many pixels contribute at large radii. The PSF must also be well-isolated, since the wings contain significant energy to a radius of 2-3 arcsec, if absolute EE is desired.

Sharpness: This is the sum of the square of the (normalized) PSF and is equivalent to the reciprocal of the number of pixels contributing to the signal in an optimally extracted image. As such it is directly applicable when determining the limiting magnitude. We have found it to be relatively sensitive to image centration for under-sampled images (such as those produced by the WFC at 633 nm) and noise (such as residual cosmic rays and flatfield features) that limit its usefulness for alignment purposes. Like the EE, it is sensitive to background subtraction error.

Phase retrieval: Fitting of the images with a model incorporating the low-order aberrations has proven most invaluable for assessing optical alignment, when high signal-to-noise ratio images can be obtained, particularly in monochromatic (e.g., HeNe laser) light. Although somewhat time-consuming compared to the other metrics discussed here, phase retrieval yields results that may be used directly to determine corrective adjustments, such as required to remove the coma due to pupil shear or to improve focus. It is insensitive to image centration. We have made extensive use of a phase retrieval package developed for HST images by C. Burrows and J. Krist.[14]

The EE was used as the primary image quality metric for most of the ground alignment of ACS, and especially for adjusting the detector tip/tilt to best match the focal surface. The latter was accomplished by obtaining a set of point source images in the RAS/HOMS HST simulator. For the WFC, nine images distributed evenly over the field were simultaneously obtained at each of 7 focus positions and the focus dependence of the EE in 0.15 arcsec diameter was computed for each field point. A fit was then generated to optimize the EE over the field and the shims required to adjust the detector focus and tip/tilt were automatically computed from the detector geometry. This technique was successful in rapidly converging to the optimal detector alignment with 2 iterations. A similar technique was used for the HRC detector although only a single field point could be illuminated at a time, rendering the results subject to thermal/mechanical drifts in the ACS or RAS/HOMS.

Table 1 presents most of the various image quality metrics described above for about 30 stars distributed over the WFC field of view. No single measurement in the table should be construed as definitive, but the ensemble may be considered an accurate representation of the overall WFC imaging performance. The low order aberration content of images obtained through the F502N filter is reported in the table in μm RMS wavefront error (WFE). All other metrics are obtained from the same star field observed through the F625W filter. No strong field dependence is apparent. The Code V model used to design the WFC optics predicts a mean aberration of .019 μm RMS, chiefly in defocus and uncorrected astigmatism. We have observed that the ACS WFC and HRC each exhibit about -.015 μm of residual 3rd-order spherical aberration, as does the WFPC2 and STIS, indicating that the true OTA differs slightly from the current prescription used to design the science instruments. The OTA also produces about .01 μm of clover, most likely due to the 3-pad mounting

of its primary mirror. Adding the OTA contribution in quadrature to the model prediction yields about .026 μm RMS WFE, in good agreement with our phase retrieval results.

Table 1. Image quality metrics over ACS/WFC field of view, filter F625W.

ID	Ctr X	Ctr Y	Pk/tot	Sharp	Wid X	Wid Y	EE(.15)	EE(.25)	Aberr
1	128	2516	0.187	0.081	0.085	0.085	0.584	0.795	0.035
2	130	723	0.216	0.085	0.078	0.079	0.578	0.800	
3	315	141	0.204	0.078	0.085	0.081	0.560	0.784	0.045
4	422	177	0.173	0.078	0.082	0.09	0.567	0.783	0.035
5	917	1281	0.217	0.094	0.071	0.083	0.603	0.811	0.030
6	930	458	0.177	0.083	0.083	0.088	0.593	0.797	0.027
7	960	599	0.216	0.088	0.076	0.080	0.586	0.802	
8	1111	1054	0.212	0.092	0.081	0.073	0.599	0.804	0.036
9	1170	2276	0.201	0.077	0.081	0.088	0.564	0.791	0.038
10	1297	700	0.172	0.087	0.085	0.085	0.606	0.802	0.029
11	1312	1437	0.204	0.086	0.081	0.083	0.595	0.804	0.042
12	1477	3551	0.185	0.090	0.084	0.076	0.600	0.808	0.024
13	1709	1089	0.239	0.096	0.071	0.077	0.617	0.826	
14	1749	2392	0.147	0.073	0.095	0.095	0.566	0.790	0.039
15	1800	684	0.217	0.094	0.07	0.083	0.601	0.804	0.034
16	1808	1441	0.217	0.085	0.076	0.083	0.581	0.802	0.042
17	1995	403	0.225	0.091	0.077	0.074	0.589	0.803	0.034
18	2063	2432	0.163	0.076	0.092	0.085	0.565	0.795	
19	2132	3722	0.179	0.087	0.085	0.083	0.605	0.802	
20	2282	2945	0.191	0.086	0.086	0.078	0.595	0.805	0.030
21	2432	2749	0.198	0.086	0.084	0.078	0.592	0.804	0.031
22	2432	1272	0.185	0.086	0.081	0.086	0.602	0.807	
23	2479	54	0.177	0.084	0.078	0.089	0.590	0.799	0.035
24	2562	1767	0.197	0.088	0.077	0.086	0.602	0.807	0.029
25	2779	75	0.208	0.085	0.081	0.078	0.584	0.796	0.031
26	2899	1926	0.184	0.088	0.085	0.077	0.606	0.810	0.028
27	2934	3099	0.175	0.087	0.077	0.088	0.602	0.803	0.027
28	3219	943	0.249	0.095	0.071	0.073	0.596	0.810	
29	3450	2764	0.201	0.083	0.083	0.080	0.582	0.797	0.040
30	3551	3445	0.137	0.079	0.089	0.093	0.587	0.794	0.031
31	3783	1134	0.213	0.086	0.076	0.081	0.588	0.799	0.035
32	4033	3738	0.211	0.080	0.077	0.087	0.563	0.786	
		Mean:	0.196	0.085	0.081	0.083	0.590	0.800	0.028

A useful indicator of possible field dependence of the image quality is shown in Figure 3, where we have plotted the 2-D gaussian-fitted FWHM, scaled by 100 to enhance visualization of any field dependence, of about 70 stars distributed over the WFC field. Variations in the spot sizes for neighboring points are indicative of the measurement errors, since any true field dependence is expected to be slowly varying with position. Multiple measurements of the same star with small pointing offsets, shown nearly overlapping in different shades, also serve to estimate the errors. No significant field dependence is apparent in this or in similar plots representing the EE and sharpness. We conclude that the WFC

detector is well-matched to the focal surface (*i.e.*, no substantial field dependence of the focus is present) and the other field-dependent aberration content is small, as predicted by the optical model.

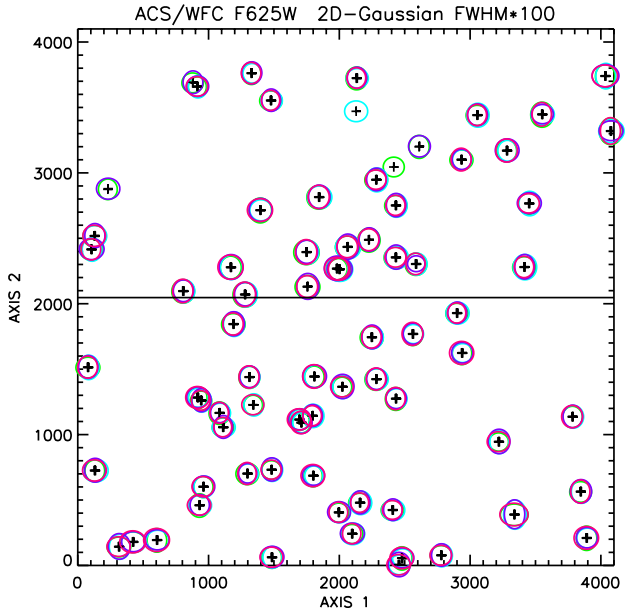

Figure 3. Measured elliptical gaussian fits to the cores of star images over the WFC field through filter F625W. The FWHM of the fits is magnified by 100. Multiple measurements with small pointing offsets are shown in 4 shades. No significant field dependence is apparent.

PSF measurements have been made at a few field points through each of the ACS filters. Figures 4 and 5 demonstrate the behavior of the EE with wavelength for the WFC and HRC, respectively. Two features are notable, both due to detector effects. The HRC EE declines above 700 nm significantly more than expected from diffraction alone, due to development of a halo produced by light transmitted through the silicon CCD and scattered by its glass substrate.[15] This effect was seen in the STIS CCD, which is very similar in construction to the HRC detector, and has been included in the model computations of Figure 5. Although the WFC CCD was modified with a halo-mitigating reflective layer, as demonstrated by its lack of a visible halo in the I band (F775W, see Figure 9), its PSF degrades substantially at wavelengths above 800 nm, due to a different form of scatter within the CCD (see sec 5. for further discussion).

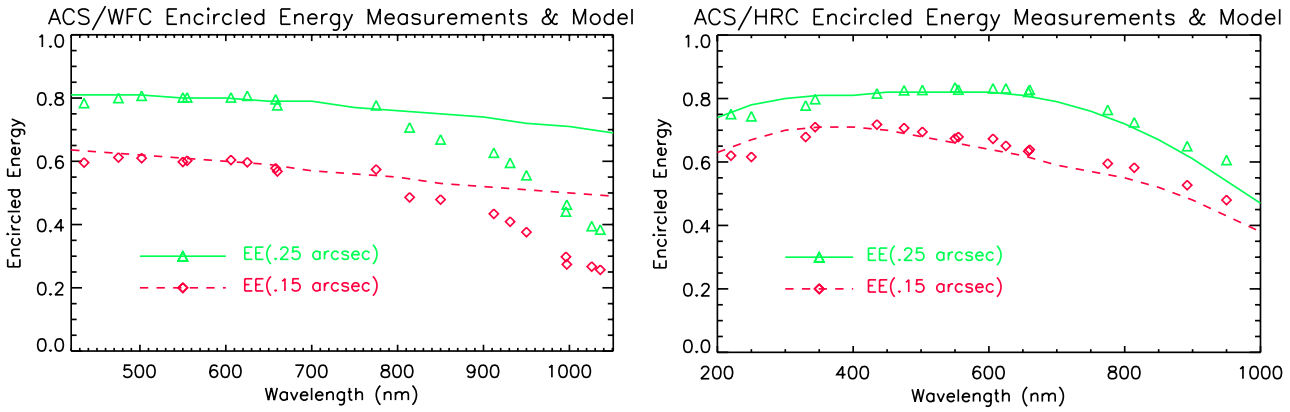

Figures 4 and 5. The measured encircled energy within diameters of 0.15 (red diamonds) and 0.25 arcsec (green triangles) are compared with model image assessments (dashed and solid lines) for the WFC and HRC.

The HRC EE also is observed to fall somewhat below expectations at the short wavelength end of its spectral range, where the PSF exhibits a noticeable "tail". This feature is independent of field position and is mimicked in the far UV SBC images, where it becomes more prevalent. Phase retrieval analysis indicates that the feature may be produced by a moderate amount of several low-order aberrations in the optical system, listed in Table 2, combined with phase maps of the OTA mirrors. Figure 6 compares the phase retrieval fit with an observed PSF at 344 nm. This level of aberration is consistent with the expected as-built optical system and has little apparent effect on the PSF at longer wavelengths. However, the SBC images at 122 nm fall slightly below their specified EE (30% within 0.1 arcsec), most likely as a combined result of this uncorrectable aberration, the large halo induced by the MAMA detector, and the mid-frequency figure error of the OTA optics. [8]

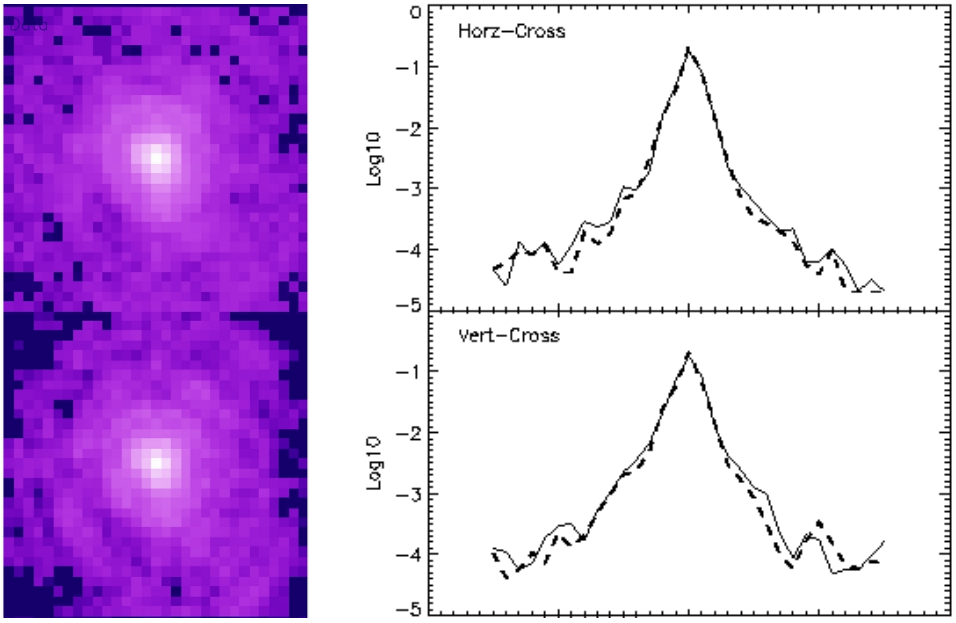

Table 2. Phase retrieval fit RMS wavefront error

Aberration	WFE (μ)
Defocus	0.007
X Coma	-0.002
Y Coma	0.003
0 Astig.	0.007
45 Astig.	-0.011
Spherical	-0.015
X Clover	0.007
Y Clover	-0.009
OTA fig err	~0.018

Figure 6. Phase retrieval fit of an HRC F344N star image. The upper left panel is the measured image, the lower left is the fit, which employed only minor levels of a few low-order aberrations and maps of the OTA figure error. The plots compare slices through the image (solid) and fit (dashed) on a log scale, indicating a reasonable fit to core and wings.

5. SCATTERED LIGHT AND GHOSTS

The ACS was designed with a requirement that no single straylight feature may contain more than 0.1% of the detected energy in the object producing it. This goal has generally been met, but a few exceptions have been identified during the extensive ground and SMOV test programs. Early testing revealed a reflection from certain areas of the CCD surface near two sides of the FOV that illuminated the back side of the knife-edged mask just in front of the CCD and scattered back to the detector, producing a spray (dubbed "dragon's breath") that exceeded the specification by an order of magnitude. Subsequent detector builds, including those integrated into the flight instrument, incorporated a redesigned mask, with the knife edges sharpened and coated black, and inverted on the offending two sides. This successfully mitigated the problem, although significant scatter from the mask can still result in special circumstances when a point source is placed just on the mask edge, as occurs in the upper right portion of Figure 7. Also prevalent in Figure 7 are a series of large annular ghosts near their parent images. These are due to reflection from the detector windows back to the filters, then returning to the CCD; the fringes arise from interference between the HeNe laser light reflections from the two surfaces of the windows. Another type of annular ghost arises from reflections between the inner and outer window

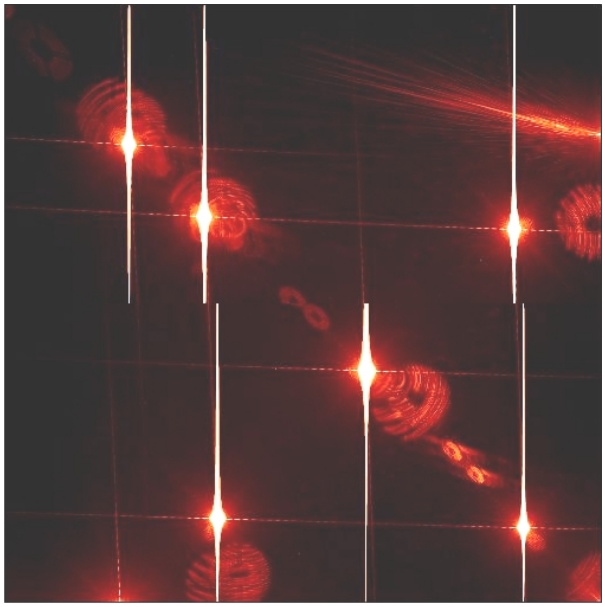

Figure 7. Straylight artifacts in the WFC

surfaces; these are much smaller in diameter, relatively low in intensity (well within the specification) and are displaced radially from the parent image by a small amount. Examples can be seen in the lower right of Figure 7.

Two optical "ghost" features have been identified that exceed the specified intensity; their origin and characteristics are well defined and they should have minimal impact on the ACS science program:

WFC elliptical haloes: Pairs of elliptical annuli, aligned along the negative diagonal of the FOV, are observed when bright sources are placed on the lower right (D amplifier) quadrant of the WFC detector. Several sets of these ghosts are apparent in Figure 7, in which 9 highly saturated point sources (note the severe charge bleeding) are placed in, and just off of, the FOV. The surface brightness of the annuli increases and size decreases with proximity to the corner. These ghosts are caused by reflection from the CCD surface (which lies at an ~20 degree angle to the chief ray) up to the detector windows and back to the CCD. Two pairs of ghosts are seen, produced by reflection from the four window surfaces. The total energy fraction in each ghost may exceed 0.2% of the target signal.

F660N ghosts: The [N II] narrow band filter produces pairs of relatively bright circular annuli stationed near to (but radially outward from) the target image. This is due to reflection from the two surfaces of the second "blocker" substrate back to the many-layer dielectric stack on the first substrate, which in turn reflects at high efficiency at the filter passband. These haloes contain ~2% of the detected target energy and are always ~ 10 and 20 px in diameter.

The gap between the two CCD chips on the WFC focal plane assembly was also a source of concern regarding scatter from bright sources placed at the abutting CCD edges or in the ~.5 mm wide gap, where residual indium solder used for chip attachment may reflect in an undesirable way. However, testing to date, though not exhaustive, has shown no significant scatter from bright point sources placed at various positions in the gap. The gap may potentially be useful to attenuate bright sources in the vicinity of fainter targets, increasing contrast and eliminating bleeding of charge from saturated images.

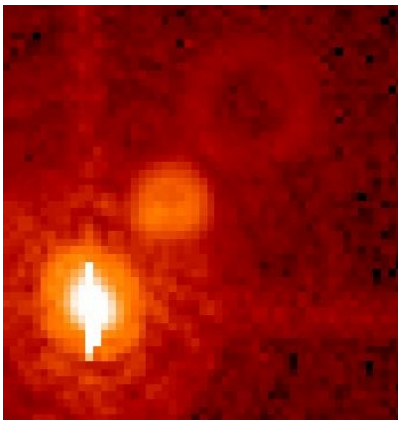

Figure 8. Filter F660N ghosts

Both ACS CCD detectors also suffer from scatter of the light that is increasingly transmitted through the silicon as wavelength increases into the near IR. The HRC CCD scatters this light into a broad halo centered on the target; the halo intensity varies strongly with wavelength and reaches about 20% of the total energy at 1 um. The WFC CCD incorporates a special anti-halation layer of reflective Al between the CCD and its glass substrate, as has been described by Sirianni, et al.[15] While this layer is effective at suppressing the IR halo, a relatively strong scatter along the CCD serial readout direction is produced at long wavelengths, as illustrated in Figure 9. We believe that this is due to scatter from the CCD channel stop structure. The feature contains about 20% of the PSF energy at 1 um, but is insignificant at 800 nm.

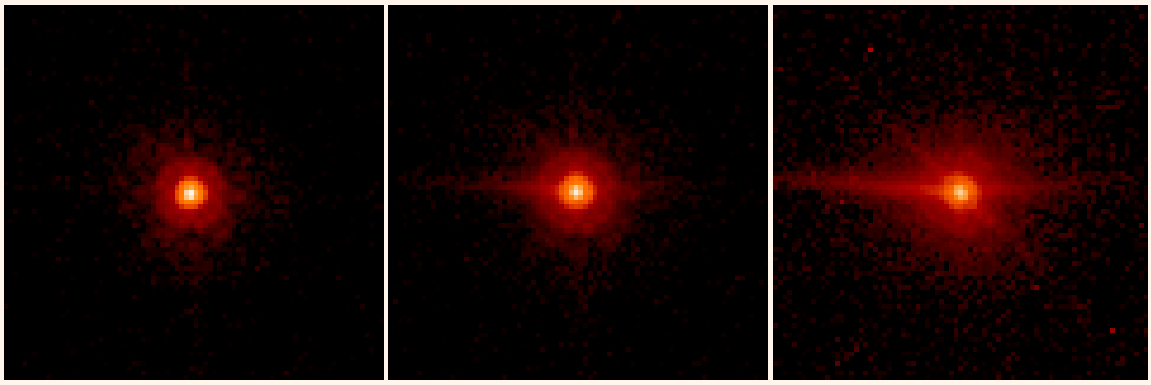

Figure 9. WFC star images through filters F775W (left), F850LP (middle), and FR1016N at 996 nm (right). The CCD scatter, undetected below ~ 800 nm, grows rapidly with longer wavelength. In addition to the asymmetrical, horizontal feature, a weaker diagonal streak also becomes apparent near 1 μm.

6. IMAGE STABILITY

The ACS design specification for image position stability for all channels requires that the OTA/ACS system maintain image drifts of less than 10 milliarcsec (mas) over two (96 minute) orbits. The rationale for this stringent requirement is to limit image smear and to permit the registration of images from consecutive orbits without resampling and the concomitant addition of noise. In practice, images are generally obtained over exposure times of <20 minutes (to limit the cosmic ray hit density) and are often "dithered" to improve spatial sampling or mitigate flat field features or sample over the WFC inter-chip gap, requiring resampling to produce the combined image. Furthermore, correction of the substantial geometric distortion requires resampling even in cases where dithering is not performed. Hence the stability specification may be viewed as overstated, and has been difficult to achieve.

Initial tests of the image stability, performed in the first ACS thermal-vacuum test in March 1999, revealed a high sensitivity of the image location to thermal changes in the structure supporting the instrument, such that the specification would clearly not be met. This behavior was traced to flexure of the bulkhead on which the M2 (asphere) mirrors were mounted, in close proximity to one of the fittings that mounts the optical bench into its enclosure. The mirror mounting was redesigned to attach to a more stable portion of the optical bench and subsequent thermal-vacuum testing demonstrated an order of magnitude improvement in image stability.

A special test was performed on-orbit to evaluate the ACS WFC and HRC image stability during a worst-case thermal slew scenario. The spacecraft was first pointed in the anti-solar direction, where the OTA and aft shroud experience the coldest conditions, for 8 orbits (~12 hrs), after which the observatory was positioned in a "hot" attitude, with an off-nominal roll to further warm the ACS side of the aft shroud. Bright stars were observed with minimal exposure times in both the HRC and WFC, with no ACS reconfiguration (except shutter rotation) for the entire duration of the test. Relative image positions were determined using cross-correlation analysis with accuracy of about 0.05 px. The results for the WFC are displayed in the left panel of Figure 10, where relative image position in the detector X (green diamonds) and Y (blue triangles) axes are separately plotted. The maximum drift rate is about 5 mas/hr, which exceeds the specification by ~50%. For reasons outlined above, and because the thermal variations encountered in normal operations are small compared to those induced by the test, we do not consider this to be of practical concern.

Higher frequency image motion (jitter) can also be assessed by examining the many sets of (10) images that were taken in rapid succession periodically throughout the test. These show peak-to-peak jitter of about 10 mas, with an RMS of about 3 mas, which is nominal for the Fine Guidance Sensors in fine lock on a moderately bright guide star pair. Evaluation of jitter on time scales of less than a second was achieved by comparing HRC exposures at its fastest shutter speed (0.1 s) with 1.0 s exposures. The image widths of the longer exposures were no larger than those of the shorter; in

fact, there is some evidence that the opposite is true, which may be due to a minor vibration induced by the shutter, which remains in constant rotation during the shortest exposures. Image widths were evaluated using the 2D-gaussian fit technique described above. The image widths of the WFC data set are plotted in the right panel of Figure 10, where the effects of the cooling and re-warming of the OTA/ACS system can be seen. Also visible is the OTA focus variation at the orbital period ("breathing"), which produces the ~5 mas amplitude oscillations seen most clearly in the X width measurements at hot attitude.

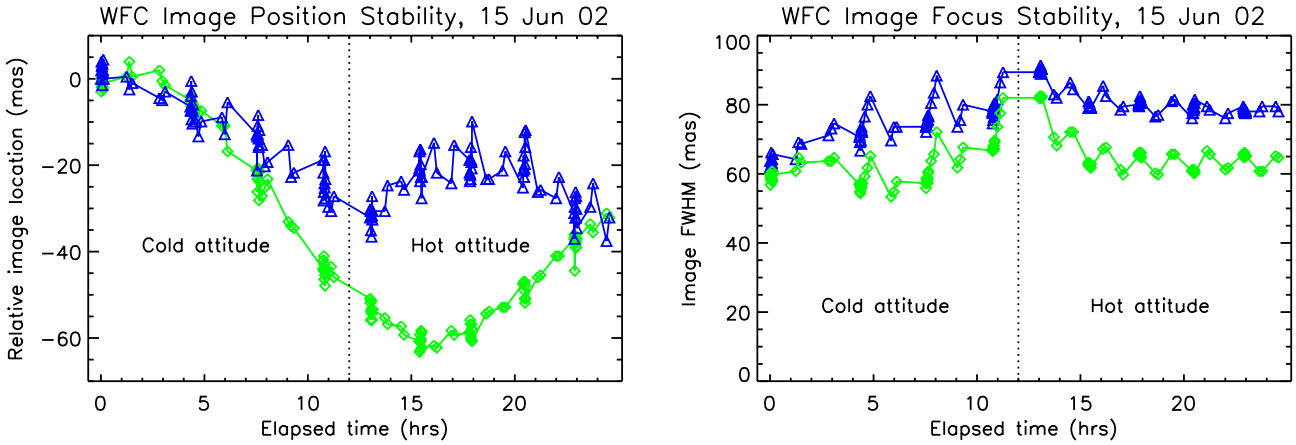

Figure 10. WFC image position (left panel) and focus (right panel) stability measured during a worst-case thermal slew.

7. ACKNOWLEDGEMENTS

ACS was developed under NASA contract NAS5-32864 and this work was supported by a NASA grant. We wish to acknowledge the support and advice of the entire ACS Science Team and the ACS group at the STScI. ACS was engineered, built and tested by a dedicated team at Ball Aerospace, Boulder, CO. The project was capably managed by the HST program at the NASA Goddard Space Flight Center, where C. Krebs and P. Sullivan stayed the course to a highly successful conclusion to a 7 year long project.

8. REFERENCES

1. Ford, H.C., and the ACS Science Team, "The Advanced Camera for the Hubble Space Telescope", *Proc SPIE* **2807**, pp 184-196, 1996.
2. Ford, H.C. and the ACS Science Team, "The HST Advanced Camera for Surveys", *Proc SPIE* **3356**, pp 234-248, 1998.
3. Ford, H.C. and the ACS Science Team, "Overview of the Advanced Camera for Surveys On-orbit Performance", *Proc SPIE* **4854**, 2002 (this volume).
4. Sirianni, M, Clampin, M, Hartig, G.F., Ford, H.C., Illingworth, G.D., Sullivan, PC., Martel, A.R., Mutchler, M., Koldewyn, W., Burmester, B., Schrein, R.J., and Argabright, V., "Characterization and Performance of ACS CCDs", *Proc SPIE* **4854**, 2002 (this volume).
5. Clampin, M. et al. "ACS Astronomical Performance", *Proc. SPIE* **4854**, 2002 (this volume).
6. Illingworth, G.D. and the ACS Science Team, "HST ACS Early Science Results", *Proc SPIE* **4854**, 2002 (this volume).
7. Krist, J.E., Golimowski, D.A., Hartig, G.F., Clampin, M and Ford, H.C., "Advanced Camera for Surveys Coronagraph on the Hubble Space Telescope", *Proc SPIE* **4860**, 2002.
8. Tran, H., Meurer, G., Ford, H.C., Martel, A., Sirianni, M., Bohlin, R., Clampin, M., Cox, C., De Marchi, G., Hartig, G., Kimble, R. and Argabright, V., "On-orbit Performance of the ACS Solar Blind Channel", *Proc SPIE* **4854**, 2002 (this volume).

9. Walsh, J., Pasquali, A. and Pirzcal, N., "The Slitless Spectrometric Mode of the ACS: Calibrations and Prospects", *Proc SPIE* **4854**, 2002 (this volume).
10. Woodruff, R.A. and Cahill, R.F., "Optical Design of the Advanced Camera for Surveys, a Third Generation HST Axial Science Instrument", *Proc SPIE* **3356**, pp 249-264, 1998.
11. Meurer, G., Lindler, D., et al., "Calibration of Geometrical Distortion in the ACS", *Proc SPIE* **4854**, 2002 (this volume).
12. Hartig, G.F., Ford, H.C., Sullivan, J.F., Gracey, R, Johnson, E., Bartko, F. and Clampin, M., "Optical Performance Verification and Calibration of the HST Advanced Camera for Surveys", *Proc SPIE* **3356**, pp 321-331, 1998.
13. Sullivan, J.F. et al., "COSTAR Refractive Aberrated Simulator (RAS) Alignment", *Proc SPIE* **1996**, pp 237-248, 1994.
14. Krist, J.E. and Burrows, C.J. "Phase-retrieval Analysis of Pre- and Post-Repair Hubble Space Telescope Images", Applied Optics, **34**, 4951, 1995.
15. Sirianni, M., et al., "Scattered Light Halos in CCDs", *Proc SPIE* **3355**, 1998.